

Article

Enhanced Mechanical Performance of a Biodegradable Fe–Mn Alloy Manufactured by Metal Injection Molding and Minor Carbon Addition

Ye Zhang ¹, Song Li ¹ , Dongyang Li ^{1,*}, Yimin Li ^{1,*} , Hao He ² and Chang Shu ²

¹ State Key Laboratory of Powder Metallurgy, Central South University, Changsha 410083, China; 193311018@csu.edu.cn (Y.Z.); ls2011sl@csu.edu.cn (S.L.)

² The Second XiangYa Hospital, Central South University, Changsha 410011, China; hehao6868@csu.edu.cn (H.H.); shuchang@csu.edu.cn (C.S.)

* Correspondence: dongyangl@csu.edu.cn (D.L.); liyimin333@csu.edu.cn (Y.L.); Tel.: +86-13319597983 (D.L.); +86-13908475507 (Y.L.)

Abstract: At present, FeMn-based degradable alloys prepared by direct sintering generally face the problems of Mn volatilization, difficult densification, and poor mechanical properties. In this work, a Fe-35Mn-0.5C alloy with low Mn volatility, high density, and favorable mechanical properties is fabricated by the metal injection molding (MIM) process. The effects of sintering pressure and minor carbon addition on microstructure and mechanical properties were studied. The corresponding mechanical deformation mechanism was discussed. The results show that a significant reduction in the proportion of Mn volatilization to less than 0.5% and higher relative density of $97 \pm 0.30\%$ are achieved in the MIM-treated Fe-35Mn-0.5C alloy by pressurized sintering at 5 atm and 0.5 wt.% carbon addition. The optimized tensile properties are attained, with an ultimate tensile strength of 772 MPa, yield strength of 290 MPa, and elongation of 35% at room temperature, which meets the mechanical needs of metallic materials for biologically implantable medical devices.

Keywords: metal injection molding; biodegradable alloys; mechanical properties



Citation: Zhang, Y.; Li, S.; Li, D.; Li, Y.; He, H.; Shu, C. Enhanced Mechanical Performance of a Biodegradable Fe–Mn Alloy Manufactured by Metal Injection Molding and Minor Carbon Addition. *Metals* **2022**, *12*, 884. <https://doi.org/10.3390/met12050884>

Academic Editors: Jingwei Zhao, Zhengyi Jiang, Leszek Adam Dobrzański and Chong Soo Lee

Received: 29 March 2022

Accepted: 11 May 2022

Published: 23 May 2022

Publisher's Note: MDPI stays neutral with regard to jurisdictional claims in published maps and institutional affiliations.



Copyright: © 2022 by the authors. Licensee MDPI, Basel, Switzerland. This article is an open access article distributed under the terms and conditions of the Creative Commons Attribution (CC BY) license (<https://creativecommons.org/licenses/by/4.0/>).

1. Introduction

Fe–Mn alloys have attracted widespread attention as biodegradable materials owing to their broad range of properties, good processability, and favorable biocompatibility [1–4]. Mn is involved in the metabolic processes of amino acids, proteins, and carbohydrates in humans, and plays an essential role in the operation of the immune system, the regulation of energy, and the growth of tissues. The studies have shown that the amount of Mn released by the degradation of FeMn-based alloys in body fluids is much lower than their toxicity level in the blood and the body can also rationally metabolize the gradual release of Mn [3,5,6]. Meanwhile, the electrode potential of Mn is lower than Fe, the infinite solid solution formed by Fe–Mn has a higher corrosion potential, and when the Mn content is higher than 29 wt.%, Fe–Mn alloys possess a single austenite phase, improving the magnetic resonance imaging (MRI) compatibility [7]. Hermawan et al. [2,7] reported the feasibility of Fe–Mn alloys as biodegradable materials. Except for elongation, the mechanical properties were superior to ASTM SS 316L. Their corrosion rates ($CR = 0.5\text{--}0.7\text{ mm/y}$) were much higher than pure iron. The alloys showed a suitable degradation behavior with a uniform corrosion mechanism and a slow release of ions. The addition of a third alloying element, such as C [8], Ag [9,10], Cu [11], and S [12], can further improve the degradation rate of FeMn-based alloys by forming local galvanic cells. C is a relatively ideal and economical element and can simultaneously improve strength and plasticity of Fe–30Mn [8].

Metal injection molding (MIM) is a widely recognized powder sintering technology successfully applied to large-scale fine parts' processing and preparation. However, direct

sintering to prepare Fe-Mn degradable alloys is an immature field, and there are no reports of the preparation of MIM Fe-Mn alloy materials for complex shapes. The direct sintered Fe-Mn-Si alloys reported by Xu et al. [13] had a relative density of only 62.9~67.7%. Dargusch et al. [14] reported the traditional powder metallurgy sintering preparation of porous Fe-(25/30/35)Mn alloys with a relative density between 78.7~86.1%, and the presence of ϵ martensite with poor performance. The reason for the difficulty of sintering process to prepare Fe-Mn alloys is that the concentration of Mn significantly impacts the phase composition and mechanical properties. However, the equilibrium vapor pressure of Mn increases sharply after the sintering temperature exceeds 1200 °C and is prone to volatilization [15]. The loss of Mn pollutes the equipment and the environment and impairs the material properties. In addition, the mechanical properties and long-term fatigue properties are limited owing to the inclusions and pores during the sintering process.

Our previous work reported the mechanical properties and degradation properties of Fe-Mn degradable alloys prepared by MIM sintering [16]. There is still a significant Mn loss (2.25%), the oxygen impurity content is high (0.32 wt.%), and the relative density is approximately 93%. The single deformation mechanism and higher porosity result in poor mechanical properties ($\sigma_s = 558$ MPa, $\epsilon = 10.8\%$), reducing such alloys' practical value. This study examines the microstructure, mechanical properties, and corresponding mechanical deformation mechanism of MIM-treated Fe-Mn alloys after optimizing the carbon content and sintering pressure. This result further provides the theoretical and experimental basis to develop complex, biomedical, degradable Fe-Mn alloy products directly by the MIM technique.

2. Materials and Methods

As shown in Figure 1a,b, the Fe-35Mn pre-alloyed ($D_{50} = 14.0$ μm) and graphite ($D_{50} = 30.8$ μm) powders used in the study were provided by Hunan Hengji Powder Technology Co., Ltd., Hunan Province, China. The raw powders were mixed uniformly in the mixer (20 rpm, 12 h). The mixed powders and a multi-component binder system (60 wt.% paraffin + 36.5 wt.% high-density polyethylene + 3.5 wt.% stearic acid) were mixed in an internal mixer (XSM1/20-80, MITR, Changsha, China) for 3 h. The loading of the powder mixtures was performed at 58 vol.%. The obtained feedstock was pelletized by a pelletizer (CFine, Dongguan, China) and injected into the green parts of the tensile samples (a length of 108 mm and a diameter of 3.8 mm, shown in Figure 1c) using an injection machine (HTF-90W2, Haitian Group, Ningbo, China). The binder was removed by a two-step debinding method involving solvent debinding (dichloromethane, 40 °C, 8 h), followed by thermal debinding (argon, 600 °C, 1 h). The injected specimens were then sintered at 1200 °C for 7 h under a low vacuum atmosphere (10^{-1} Pa) or under an argon atmosphere at the applied pressure of 5 atm. The selection of the sintering temperature and holding time mainly refers to the equilibrium vapor pressure of Mn and the results of our previous study [15,16]. As shown in Figure 1c, the length shrinkage rate and radial shrinkage rate of the sintered parts were 13.26% and 14.14%, respectively. The main sintering parameters are depicted in Table 1. The Fe-35Mn alloys obtained by low vacuum and pressure sintering were labeled as VS and PS alloys, respectively, while the Fe-35Mn-0.5C alloy prepared by pressure sintering was called as PS0.5 alloy.

The relative density of the sintered specimens was measured by the Archimedes method using electronic balance and was conducted eight times to determine the average value. The Mn content was analyzed using an inductively coupled plasma mass spectrometer (ICP-MS, Thermo Fisher Scientific, Massachusetts, USA). The C and O contents were analyzed using a CS-600 carbon sulfur analyzer and a TCH-600 oxygen, nitrogen, and hydrogen analyzer, respectively. Phase identification was performed by the X-ray diffractometer (XRD, D8 Advance, Bruker (Beijing) Scientific Technology Co. Ltd., Beijing, China) with Cu K α radiation ($\lambda = 1.5418$ Å) at a scanning rate of 6°/min operated at 40 kV and 40 mA. The slices obtained by wire cutting from the sintered samples were grinded (abrasive papers with various degrees of roughness: 180~2000 #), mechanically polished (SiO₂ suspension), and then observed using a scanning electron microscope (SEM, Quanta

FEG 250, FEI, Hillsboro, OR, USA) with an energy dispersive spectrometer (EDS, Quanta 450F, FEI, Hillsboro, OR, USA) analyzer. The samples for transmission electron microscope (TEM, Tecnai G2 F20, FEI, Hillsboro, OR, USA) observation and electron backscatter diffraction (EBSD, Helios Nanolab G3 UC, FEI, Hillsboro, OR, USA) analysis were machined to a thickness of 50~60 μm and then electro-polished using an electrolyte composed of 10% perchloric acid and 90% ethanol (25 V, 15 mA, $-30\text{ }^{\circ}\text{C}$). The EBSD scanning was performed with a step size of 1.5 μm , and the data were analyzed by orientation imaging microscopy (OIM) software. The tensile tests were carried out using an electronic universal material tester (3369, Instron, Norwood, MA, USA) with a speed of 2 mm/min at room temperature and the tensile strain was corrected by a gauge extensometer. The tests were conducted at least three times for each sample to determine the average value.

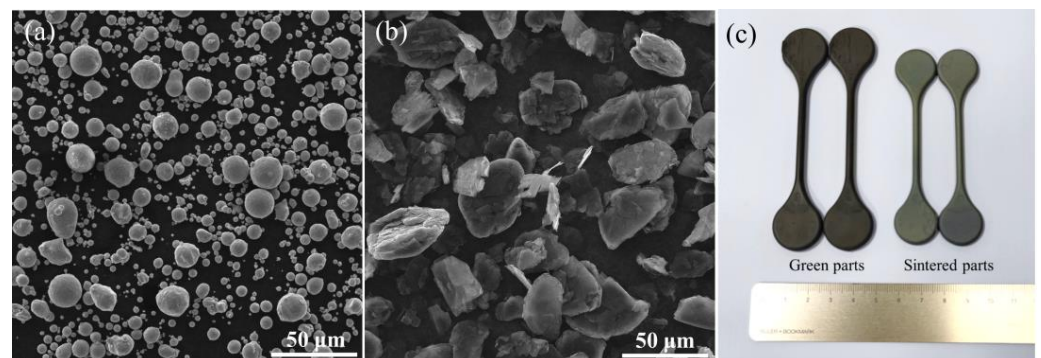


Figure 1. SEM morphology of (a) the pre-alloyed Fe-35Mn powder and (b) graphite powder; (c) injection green parts and sintered parts of the tensile samples.

Table 1. The main sintering parameters of the VS, PS, and PS0.5 alloys.

Samples	Temperature ($^{\circ}\text{C}$)	Time (h)	Atmosphere	Pressure
Fe-35Mn (VS)	1200	7	vacuum	10^{-1} Pa
Fe-35Mn (PS)	1200	7	argon	5 atm
Fe-35Mn-0.5C (PS0.5)	1200	7	argon	5 atm

3. Results and Discussion

3.1. Microstructure and Phase Characterization

Table 2 shows the content of major alloying elements and the relative density of the VS, PS, and PS0.5 alloys. Although the sintering pressure was different, the carbon and oxygen contents were similar for the VS and PS alloys without any addition of carbon. The loss of Mn under pressure sintering was lower than vacuum sintering. Although the equilibrium vapor pressure of Mn was similar at the same temperature, a small amount of volatilized Mn vapor was continuously evacuated under the vacuum system, promoting the continuous loss of Mn during the sintering process. However, this problem can be avoided in pressurized environments. This dramatically reduces the volatilization of Mn and ensures the stability of the alloy composition. Simultaneously, the relative density of the PS alloy under a pressurized environment was significantly higher than the VS alloy. The addition of carbon reduced the liquid temperature of iron-based materials, increased the diffusion rate, and increased the sintered density in the PS0.5 alloy.

Table 2. The element content and relative density of the VS, PS, and PS0.5 alloys.

Samples	C (wt.%)	O (wt.%)	Mn (wt.%)	Ratio of Mn Loss (%)	Relative Density (%)
VS	0.05	0.35	32.21 ± 0.14	2.79	93.1 ± 0.12
PS	0.08	0.31	34.46 ± 0.11	0.54	95.0 ± 0.34
PS0.5	0.46	0.08	34.54 ± 0.15	0.46	97.0 ± 0.30

Figure 2 shows the XRD patterns of the VS, PS, and PS0.5 alloys. The phase composition of the alloys was uniform and consisted of a single austenite. The positions of diffraction peaks of the VS and PS alloys were the same, and the diffraction peaks of the PS0.5 alloy shifted to the left owing to the interstitial solid solution of carbon.

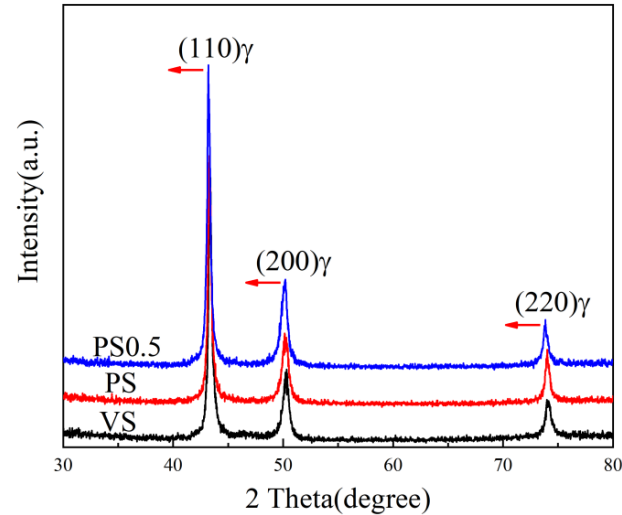


Figure 2. The XRD patterns of the sintered alloys.

Figure 3 illustrates the microstructure and EDS analysis of the VS, PS, and PS0.5 alloys. The porosity of the alloys reflected the change in the density. The VS alloy had pores of varying sizes and irregular shapes, while the pores of the PS and PS0.5 alloys were fine and uniform. The EDS results showed that the grey impurity phase in the VS and PS alloys was mainly composed of MnOx.

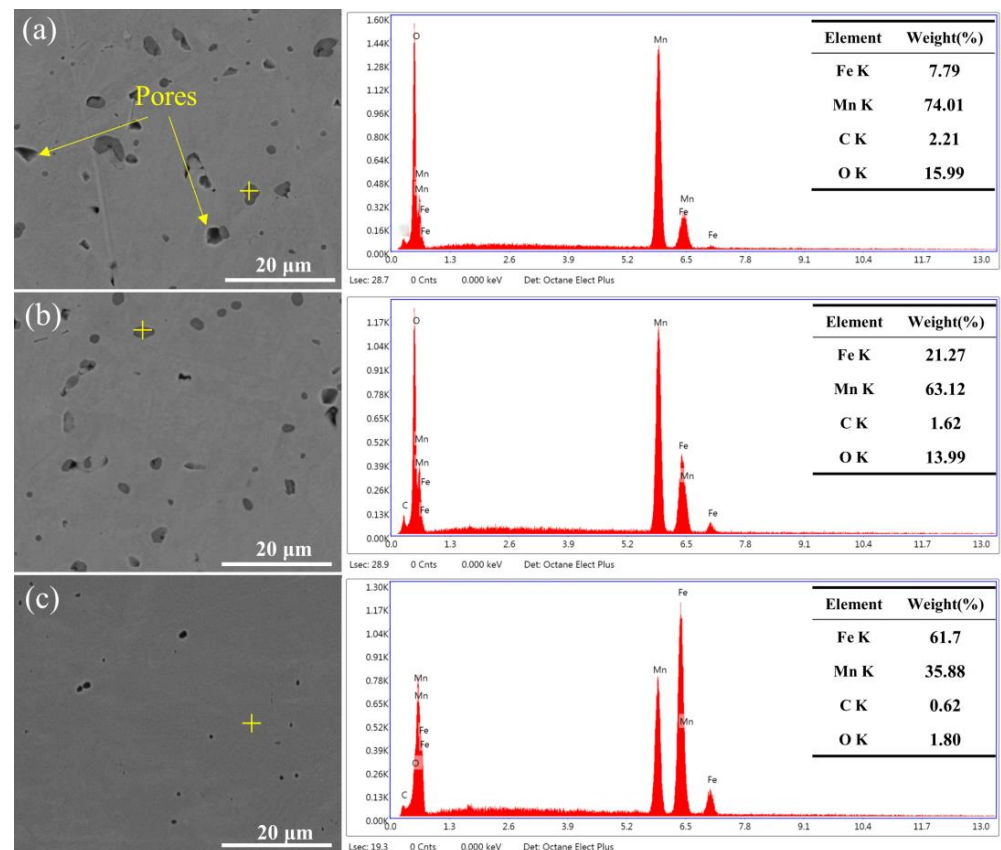


Figure 3. SEM images and EDS analysis of alloys: (a) VS; (b) PS; (c) PS0.5.

3.2. Mechanical Properties

Figure 4a exhibits the room-temperature tensile stress–strain curves of the VS, PS, and PS0.5 alloys. The VS alloy had an ultimate tensile strength of 355 MPa and an elongation of 11%. The PS alloy had an ultimate tensile strength of 510 MPa and an elongation of 25%. The tensile strength of the PS0.5 alloy was further increased to 778 MPa, and the elongation was increased to 35% by adding 0.5 wt.% carbon. It can be observed that the strength and plasticity were simultaneously improved with the optimization of the sintering atmosphere and carbon content. The significant increase in strength was attributed to the increase in the density, the reduction in porosity, and the solid solution strengthening of carbon (consistent with the peak shift in XRD). The changes in plasticity are discussed in Section 3.3. The SEM images of the fracture surface of the VS, PS, and PS0.5 alloys are shown in Figure 5. All alloys exhibited ductile fracture characteristic, in which deeper and larger dimples began to appear as the plasticity of the alloys increased. This was consistent with the results of the mechanical properties.

Figure 4b shows the comparison between the tensile mechanical properties of the VS, PS, and PS0.5 alloys and the biodegradable Fe-Mn, Mg, and Zn alloys reported in the main the literature [17–24]. Compared with Mg alloys, the relatively dense Fe alloys had a better strength and ductility. Zn alloys had a good plasticity and poor strength. The high-performance MIM-treated PS0.5 alloy obtained by pressure sintering and micro-alloying carbon in this study demonstrated better mechanical properties than the dense Fe-35Mn prepared by Hermawan et al. The strength of the alloy was also higher than that of ASTM 316 L stainless steels with a similar plasticity [7].

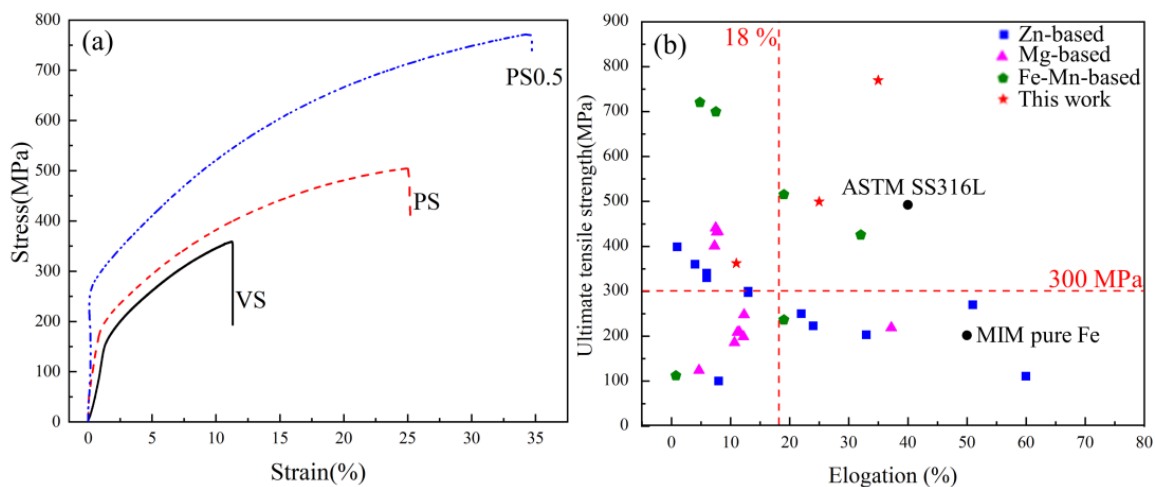


Figure 4. (a) The tensile stress–strain curve and (b) comparison of the comprehensive mechanical properties with the biodegradable Fe-Mn, Mg, and Zn alloys reported in the main the literature [17–24].

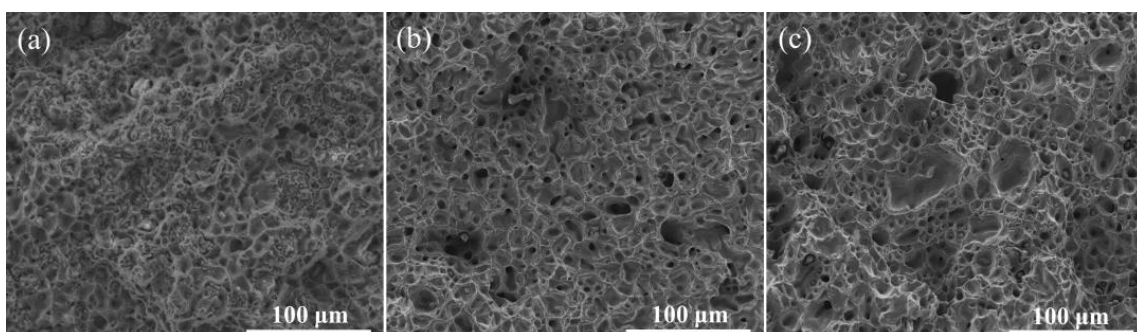


Figure 5. The fracture surface of the alloys: (a) VS; (b) PS; (c) PS0.5.

3.3. Deformation Mechanism Analysis

It has been found that twinning-induced plasticity frequently occurs in high manganese austenitic steel with a low stacking fault energy. This is the primary mechanism for improving the strength and plasticity of this material [25–27]. Figure 6a–c shows the EBSD image quality (IQ) and inverse pole figures (IPF) of the VS, PS, and PS0.5 alloys at a tensile strain of 10%. Figure 6d exhibits the percentage of twins in these three alloys. As shown in Figure 6a, a small number of twins were observed in the VS alloy. A larger number of twins began to appear in the PS alloy (Figure 6b). It has been reported that the increase in the number and the formation rate of twins is attributed to the increase in Mn content [28]. This type of twin penetrates the inside of the grains and divides the austenite grains. These intragranular substructures effectively strengthen the matrix and improve plasticity. The pressurized densification and twinning-induced plasticity mechanisms synergistically enhanced the strength and plasticity of the alloys. Compared with the PS alloy, the minor addition of carbon led to an increase in the grain size of the PS0.5 alloy with a decrease in the number of twins. This may be attributed to the suppression of the formation of initial deformation twins due to the increase in stacking fault energy (SFE) resulting from the carbon addition [29–31].

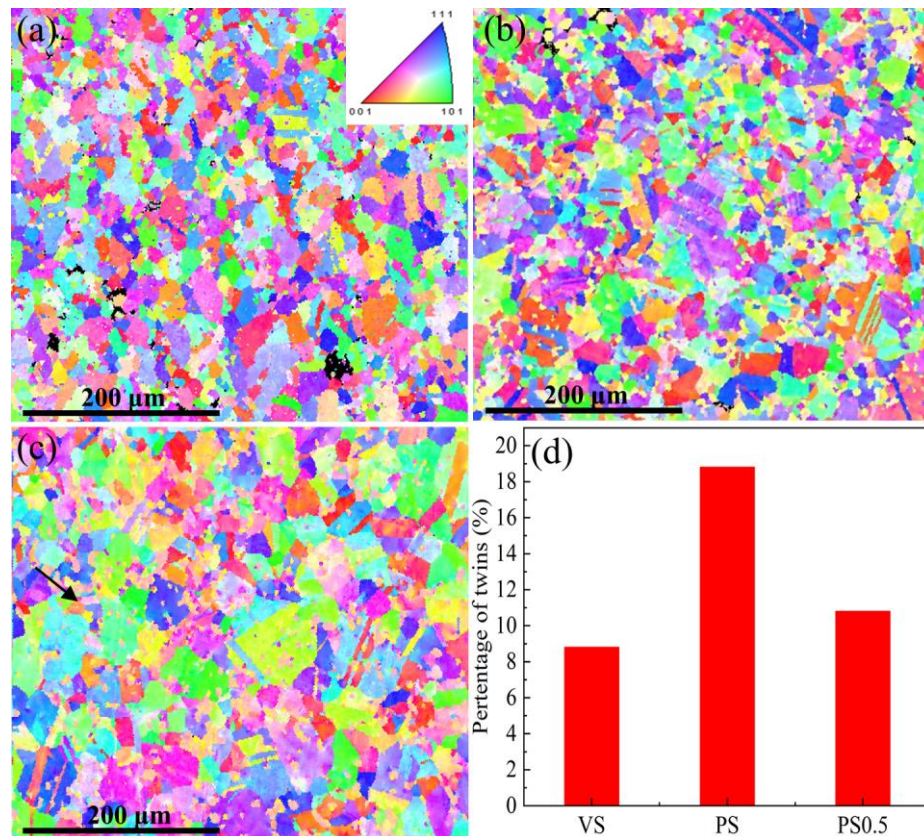


Figure 6. The EBSD IPF diagram of alloys at 10% tensile strain: (a) VS, (b) PS, (c) PS0.5; (d) the percentage of twins.

Figure 7 shows the typical TEM bright-field images and the selected electron diffraction patterns of the VS, PS, and PS0.5 alloys deformed to a tensile strain of 10%. As shown in Figure 7a–c, a small number of twins were observed for the three alloys. The twins in different directions appeared in the PS alloy (Figure 7b). The interaction between twins is beneficial for improving the strength and ductility of the alloys. The PS0.5 alloy displayed a single direction of twins due to the increase in SFE (Figure 7c). Despite the presence of carbon delaying the appearance of deformation twins, it has been shown that the formation rate of twins increases with increasing carbon content as the strain continues

to increase [32,33]. This helps to increase the strength and plasticity of the PS0.5 alloy and will be studied in the future work. Notably, the addition of 0.5 wt.% carbon also enabled the reduction of Fe and Mn oxide, leading to the improvement in the strength and ductility of the alloy.

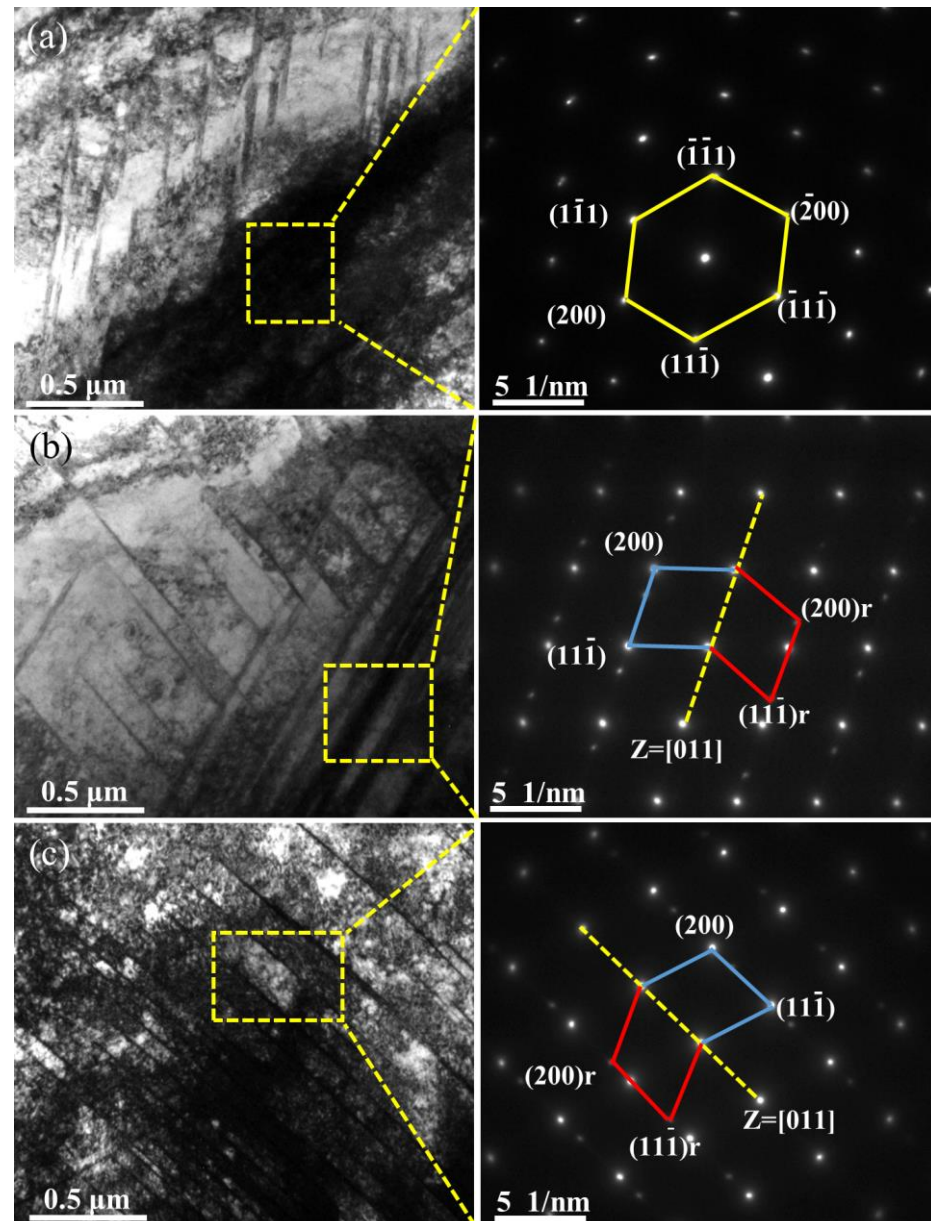


Figure 7. The TEM bright-field images and selected electron diffraction of alloys at 10% tensile strain: (a) VS; (b) PS; (c) PS0.5.

4. Conclusions

In this paper, a Fe-35Mn biodegradable alloy was prepared by metal injection molding. After optimizing the sintering environment and 0.5 wt.% carbon addition, the microstructure changes, mechanical properties, and corresponding deformation mechanisms were studied. The following conclusions can be highlighted:

- (1) Compared to vacuum sintering, even though the Mn equilibrium vapor pressure is the same, Mn loss under pressure sintering can be significantly reduced to less than 0.5% because the pressure system avoids the continuous extraction of Mn vapor. The

relative density of the Fe-35Mn-0.5C alloy was enhanced to $97 \pm 0.30\%$ by increasing the sintering pressure and adding carbon content.

- (2) With the addition of trace carbon and optimization of the sintering process, the tensile strength and elongation were simultaneously improved significantly. The ultimate tensile strength of 772 MPa in PS0.5, yield strength of 290 MPa, and elongation of 35% are much higher than those of the directly sintered Fe-35Mn alloys previously reported in the literature. The highly dense microstructure, uniform austenite phase composition, twinning-induced plasticity, and carbon-accelerated twin growth mechanism are responsible for the excellent mechanical properties.

Author Contributions: Conceptualization, Y.Z. and D.L.; Methodology, Y.Z. and D.L.; Validation, Y.Z. and D.L.; Investigation, Y.Z. and D.L.; Resources, Y.L., S.L., H.H. and C.S.; Data Curation, Y.Z.; Writing—Original Draft Preparation, Y.Z. and D.L.; Writing—Review and Editing, D.L. and S.L.; Supervision, Y.L. and S.L.; Funding Acquisition, Y.L. and S.L. All authors have read and agreed to the published version of the manuscript.

Funding: The authors acknowledge the support from Major Projects of Changsha Science and Technology Plan (Grant No. kh2003014 and kq2102003) and Graduate Research and Innovation Project of Central South University (202191001).

Institutional Review Board Statement: Not applicable.

Informed Consent Statement: Not applicable.

Data Availability Statement: Not applicable.

Conflicts of Interest: The authors declare no conflict of interest.

References

- Liu, P.F.; Zhang, D.C.; Dai, Y.L. Microstructure, mechanical properties, degradation behavior, and biocompatibility of porous Fe-Mn alloys fabricated by sponge impregnation and sintering techniques. *Acta Biomater.* **2020**, *114*, 485–496. [CrossRef] [PubMed]
- Hermawan, H.; Dubé, D.; Mantovani, D. Development of degradable Fe-35Mn Alloy for biomedical application. *Adv. Mater. Res.* **2007**, *15–17*, 107–112.
- Hermawan, H.; Purnama, A.; Dubé, D. Fe–Mn alloys for metallic biodegradable stents: Degradation and cell viability studies. *Acta Biomater.* **2010**, *6*, 1852–1860. [CrossRef] [PubMed]
- Sing, N.B.; Mostavan, A.; Hamzah, E. Degradation behavior of biodegradable Fe35Mn alloy stents. *J. Biomed. Mater. Res. B* **2015**, *103*, 572–577. [CrossRef] [PubMed]
- Jynge, P.; Brurok, H.; Asplund, A. Cardiovascular safety of MnDPDP and MnCl₂. *Acta Radiol.* **1997**, *38*, 740–749. [CrossRef]
- Crossgrove, J.; Zheng, W. Manganese toxicity upon overexposure. *NMR Biomed.* **2004**, *17*, 544–553. [CrossRef]
- Hermawan, D.; Dubé, D.; Mantovani, D. Degradable metallic biomaterials: Design and development of Fe-Mn alloys for stents. *J. Biomed. Mater. Res. A* **2010**, *93*, 1–11. [CrossRef]
- Xu, W.L.; Lu, X.; Tan, L.L. Study on properties of a novel biodegradable Fe-30Mn-1C alloy. *Acta Metall. Sin.* **2011**, *47*, 1342–1347.
- Liu, R.Y.; He, R.G.; Chen, Y.X. Effect of Ag on the microstructure, mechanical and bio-corrosion properties of Fe–30Mn Alloy. *Acta Metall. Sin.* **2019**, *32*, 1337–1345. [CrossRef]
- Sotoudehbagha, P.; Sheibani, S.; Khakbiz, M. Novel antibacterial biodegradable Fe-Mn-Ag alloys produced by mechanical alloying. *Sci. Eng. Compos. Mater.* **2018**, *88*, 88–94. [CrossRef]
- Mandal, S.; Ummadi, R.; Bose, M. Fe-Mn-Cu alloy as biodegradable material with enhanced antimicrobial properties. *Mater. Lett.* **2019**, *237*, 323–327. [CrossRef]
- Hufenbach, J.; Wendrock, H.; Kochta, F. Novel biodegradable Fe-Mn-C-S alloy with superior mechanical and corrosion properties. *Mater. Lett.* **2017**, *186*, 330–333. [CrossRef]
- Xu, Z.G.; Hodgson, M.A.; Cao, P. A comparative study of powder metallurgical (PM) and wrought Fe-Mn-Si alloys. *Mater. Sci. Eng. A* **2015**, *630*, 116–124. [CrossRef]
- Dargusch, M.S.; Manshadi, A.D.; Shahbazi, M. Exploring the role of Manganese on the microstructure, mechanical properties, biodegradability, and biocompatibility of porous iron-based scaffolds. *ACS Biomater. Sci. Eng.* **2019**, *5*, 1686–1702. [CrossRef] [PubMed]
- Hou, S.L. Vapourization and control of manganese in vacuum induction melting. *Shanghai Metal.* **1992**, *2*, 60–61.
- Zhang, Y.; Li, D.Y.; Li, Y.M. Preparation and properties of biodegradable Fe-Mn alloy by injection molding. *Mater. Sci. Eng. Powder. Metall.* **2022**, *1*, 102–110.
- Kubásek, J.; Vojtěch, D.; Jablonská, E. Structure, mechanical characteristics and in vitro degradation, cytotoxicity, genotoxicity and mutagenicity of novel biodegradable Zn-Mg alloys. *Mater. Sci. Eng. C* **2016**, *58*, 24–35. [CrossRef]

18. Niu, J.L.; Tang, Z.B.; Huang, H. Research on a Zn-Cu alloy as a biodegradable material for potential vascular stents application. *Mater. Sci. Eng. C* **2016**, *69*, 407–413. [[CrossRef](#)]
19. Gong, H.B.; Wang, K.; Strich, R. In vitro biodegradation behavior, mechanical properties, and cytotoxicity of biodegradable Zn-Mg alloy. *J. Biomed. Mater. Res. B* **2015**, *103*, 1632–1640. [[CrossRef](#)]
20. Mostaed, E.; Sikora-Jasinska, M.; Mostaed, A. Novel Zn-based alloys for biodegradable stent applications: Design, development and in vitro degradation. *J. Mech. Behav. Biomed.* **2016**, *60*, 581–602. [[CrossRef](#)]
21. Li, H.; Peng, Q.M.; Li, X.J. Microstructures, mechanical and cytocompatibility of degradable Mg-Zn based orthopedic biomaterials. *Mater. Des.* **2014**, *58*, 43–51. [[CrossRef](#)]
22. Zhang, X.B.; Zhang, Y.; Chen, K. Microstructure, mechanical and corrosion properties of Mg-Nd-Zn-Sr-Zr alloy as a biodegradable material. *Mater. Sci. Tech-Lond.* **2015**, *31*, 866–873. [[CrossRef](#)]
23. Geng, Z.W.; Xiao, D.H.; Chen, L. Microstructure, mechanical properties, and corrosion behavior of degradable Mg-Al-Cu-Zn-Gd alloys. *J. Alloys Compd.* **2016**, *686*, 145–152. [[CrossRef](#)]
24. Zhang, X.; Xue, Y.; Wang, Z. Microstructure, mechanical and corrosion properties of Mg-(4-x) Nd-x Gd-Sr-Zn-Zr biomagnesium alloys. *Acta. Metall. Sin.* **2014**, *50*, 979–988.
25. Bouaziz, O.; Allain, S.; Scott, C.P. High manganese austenitic twinning induced plasticity steels: A review of the microstructure properties relationships. *Curr. Opin. Solid State Mater. Sci.* **2011**, *15*, 141–168. [[CrossRef](#)]
26. Idrissi, H.; Renard, K.; Ryelandt, L. On the mechanism of twin formation in Fe-Mn-C TWIP steels. *Acta. Mater.* **2010**, *58*, 2464–2476. [[CrossRef](#)]
27. Allain, S.; Chateau, J.P.; Bouaziz, O. A physical model of the twinning-induced plasticity effect in a high manganese austenitic steel. *Mater. Sci. Eng. A* **2004**, *387–389*, 143–147. [[CrossRef](#)]
28. Li, D.D.; Qian, L.H.; Liu, S. Effect of manganese content on tensile deformation behavior of Fe-Mn-C TWIP steels. *Acta. Metall. Sin.* **2018**, *12*, 1777–1784.
29. Allain, S.; Chateau, J.P.; Bouaziz, O. Correlations between the calculated stacking fault energy and the plasticity mechanisms in Fe-Mn-C alloys. *Mater. Sci. Eng. A* **2004**, *387–289*, 158–162. [[CrossRef](#)]
30. Salishchev, G.A.; Yurchenko, N.; Chernichenko, R.S. Effect of thermomechanical processing on microstructure and mechanical properties of the carbon-containing CoCrFeNiMn high entropy alloy. *J. Alloys Compd.* **2017**, *693*, 394–405.
31. Wu, Z.; Parish, C.M.; Beihjo, A. Nano-twin mediated plasticity in carbon-containing FeNiCoCrMn high entropy alloys. *J. Alloys Compd.* **2015**, *647*, 815–822. [[CrossRef](#)]
32. Peng, X. *The Effect of Carbon Content on the Stacking Fault Energy and Twinning-Induced Plasticity Behavior and Fe-Mn-Cu-C TWIP Steel*; University of Fuzhou: Fuzhou, China, 2013.
33. Peng, X.; Zhu, D.Y.; HU, Z.M. Effect of carbon content on microstructure and mechanical properties of Fe-Mn-Cu-C TWIP Steels. *Iron Steel* **2013**, *48*, 55–61.